SS12: Paramagnetic Resonance

A. Kulanthaivelu
University College

1 Abstract

The effects of electron paramagnetic resonance (EPR) are observed in a sample of ruby crystal, Al_2O_3 doped with Cr^{3+} ions. We measure the resonance field for different orientations of the crystal relative to an applied magnetic field and combine the measurements of the applied magnetic field and orientation angle at each resonance to produce a plot of the resonance field as a function of orientation. We compare measurements with a plot predicted by a theoretical model and find good agreement when the crystal axis is inclined at an angle of $\theta = (66.5 \pm 1)^{\circ}$ to the plane of the magnetic field and we then determine which energy level transition each resonance corresponds to.

2 Introduction

The paramagnetic behaviour of the ruby crystals is important on account of its applicability to the three-level solid-state maser since it has a desirable set of properties. Ruby has excellent heat conductivity at low temperatures, allowing for handling of relatively high microwave power dissipation, long sections of ruby can be grown quite easily to very close tolerances, which is necessary for the travelling-wave maser, and the ruby can be bonded to metals allowing for a high degree of versatility in maser structural design.

To predict the operating condition of this material in a three-level solid-state maser we need to know the separation of energy levels for supplying the proper pump and signal frequencies, the order of magnitude of the associated transition probabilities and other conditions such as the coincidence of transition frequencies which, by spin-spin interaction, may lead to shortening of the associated relaxation time. In our experiment we will analyse the behaviour of the energy levels of the Cr^{3+} ion within a ruby crystal by observing the effects of EPR in the sample.

2 Theory of Paramagnetic Resonance

Electron paramagnetic resonance is a technique for studying materials with unpaired electrons where the energy of photons is brought into resonance with the separation of atomic or electronic energy levels, with the splitting caused by an applied magnetic field, so that absorption takes place.

In ordinary paramagnetic resonance we consider atoms with a finite magnetic dipole moment interacting with an externally applied magnetic field. The energy of a dipole in a magnetic field is given by

$$U = -\mathbf{m} \cdot \mathbf{B} \tag{1}$$

Classically, this implies we could obtain a continuum of values between $\pm m_J B$, but, since angular momentum is quantised, we find that

$$U = -m_J g \mu_B B, \qquad m_J = -J, -J+1, \dots, J-1, J \tag{2}$$

where J refers to the total orbital angular momentum.

EPR induces magnetic dipole transitions between these quantised energy levels using radiation of frequency ν. To first order each transition between energy levels must obey the selection rule $\Delta m_J = \pm 1$. In this case we obtain the resonance condition

$$h\nu = \Delta U = \left(\left|m_J \pm 1\right| - \left|m_J\right|\right) g\mu_B B = g\mu_B B \tag{3}$$

EPR spectra can be generated by either varying the photon frequency incident on a sample while holding the magnetic field constant or doing the reverse. In practice, it is usually the frequency that is kept fixed and this is the procedure we have adopted in our experiment.

By increasing an external magnetic field, the gap between the energy states is widened until it matches the energy of the microwaves. At this point the unpaired electrons can move between their two spin states. Since there typically are more electrons in the lower state, due to the Maxwell–Boltzmann distribution, there is a net absorption of energy, and it is this absorption that is monitored and converted into a spectrum.

Figure 1 shows the relationship between the absorption spectrum and observed EPR spectrum. The upper spectrum is the simulated absorption for a system of free electrons in a varying magnetic field. The lower spectrum is the first derivative of the absorption spectrum. The latter is what we measure and the most common way to record and publish EPR spectra.

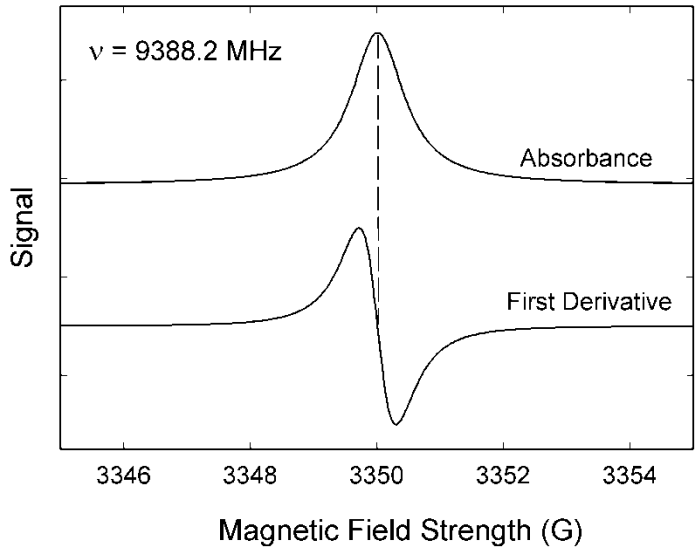

Figure 1: Diagram showing the relationship between absorption signal and the measured signal (first derivative)

3 The Spin Hamiltonian for Ruby

To describe the behaviour of the energy levels of the Cr^{3+} ion we need to have a form for the spin Hamiltonian of the system. Briefly, the spin Hamiltonian describes the energy of a paramagnetic ion arising from interaction with host crystal environment and applied magnetic field. A complete derivation of the spin Hamiltonian has been provided in appendix B.

The system of interest is the trivalent chromium ion substituted into the $\alpha - Al_2O_3$ corrundum lattice in a normal aluminium site. The basic structure is rhombohedral in which all Cr and Al atoms are in equivalent sites with trigonal symmetry, as can be seen in figure 2; consequently the internal electric fields also have trigonal symmetry about the crystallographic axis.

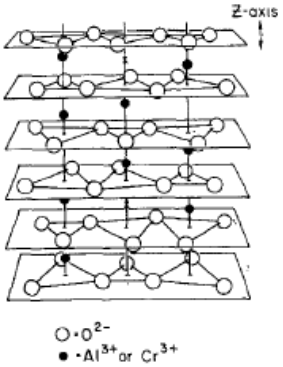

Figure 2: Pictorial view of the $\alpha - Al_2O_3$ lattice, showing z axis and ionic sites

For the present case the ground orbital state is the only one populated at room temperatures since the first excited state is approximately 1 eV higher in energy. The free Cr^{3+} ion has a ground-state multiplet described in Russel-Saunders notation as ${}^4F_{3/2}$. This comes from an electronic configuration of three $3d$ electrons. However, within the Al_2O_3 lattice the trivalent chromium ion is subjected to strong electric fields, being strongly repelled by the negative oxygen ions which surround the chromium site, and this perturbs the energy levels. The electrons then take on a new configuration in which the ground state minimises the average value of the crystalline potential energy, since the normally seven fold degenerate ground orbital states corresponding to the $2L + 1$ orbital states for $L = 3$ are no longer eigenstates of the ionic Hamiltonian.

We can still consider the chromium ion to be an eigenstate of spin since the crystal field has little effect on electron spin, with the only modification being an indirect one through the mechanism of spin-orbit coupling which generates a very small splitting. The ground orbital state, therefore, retains four fold spin degeneracy. These spin levels are the subject of interest in the EPR problem.

The two terms describing the effects of the magnetic field and the crystalline electric field can be added to produce a resultant spin Hamiltonian which provides a complete description of all aspects of the static and dynamic behaviour of the four spin levels under the application of both static and time-dependent magnetic fields.

$$H = g\mu_B \mathbf{B} \cdot \mathbf{S}' - D\left(S_z^2 - \frac{5}{4}\right) \tag{4}$$

In general g would be a tensor, having different values depending upon whether the applied field is parallel to the crystal axis or perpendicular to it. This modification of the ordinary landé g-factor is due to the indirect effect of the spin-orbit coupling. As demonstrated by Schulz-Dubois[1] the values of $g_\perp$ and $g_\parallel$ are roughly the same and so in our experiment we treat g as a scalar.

In the representation $|i\rangle = |s, m_i\rangle$ this gives us the required Hamiltonian in matrix form which we diagonalise to find the energies and eigenstates. This generates the secular equation

$$E_n^4 - E_n^2\left[2D^2 + \frac{5}{2}(g\mu_B B)^2\right] + 2DE_n(g\mu_b B)^2(3\cos^2\theta\cos^2\phi - 1) + D^4 + \frac{9}{16}(g\mu_B B)^4 + \frac{1}{2}D^2(g\mu_B B)^2(1 - 6\cos^2\theta\cos^2\phi) = 0 \quad (5)$$

Where the angles θ and ϕ correspond to the angle of inclination to the magnetic field and the orientation angle respectively as shown in figure 3.

Solving this equation we obtain the energy eigenvalues as a function of magnetic field and orientation angle.

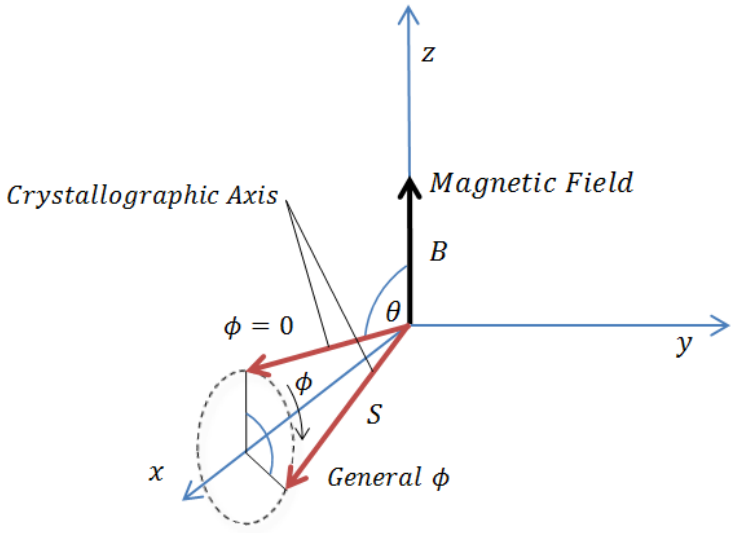

Figure 3: Effective vector model representation of rotating the sample in our experiment

4 Experimental Arrangement and Measurements

A Gunn diode, emitting in the X-band, was used as a source of photons. The photons travel down a rectangular waveguide past various millimetre-wave components. These components included a wavemeter, needed to determine the photon frequency, a monitor diode, which is used to monitor the power from the Gunn diode, and an attenuator to attenuate the power.

The photons then enter a resonant cavity containing the sample under study. The cavity had a very high Q-factor to enhance the sensitivity of the apparatus to the rather weak EPR signal. Because of this the cavity required careful mechanical tuning with the effective size of the cavity varied in such a way as to make its resonant frequency coincide with the frequency emitted by the Gunn.

The resonant cavity was between the pole pieces of an electromagnet, the field of which may be swept in order to observe EPR. In addition, an NMR and Hall probe were located between the pole pieces to enable accurate measurements of the magnetic field to be made by observing the nuclear magnetic resonance of protons in water. Nuclear magnetic resonance of protons occurs at 42.5759 MHzT^{-1} so that if we know the frequency at which NMR of protons occurs at the same field as the EPR , the magnetic field can in principle be determined to great accuracy.

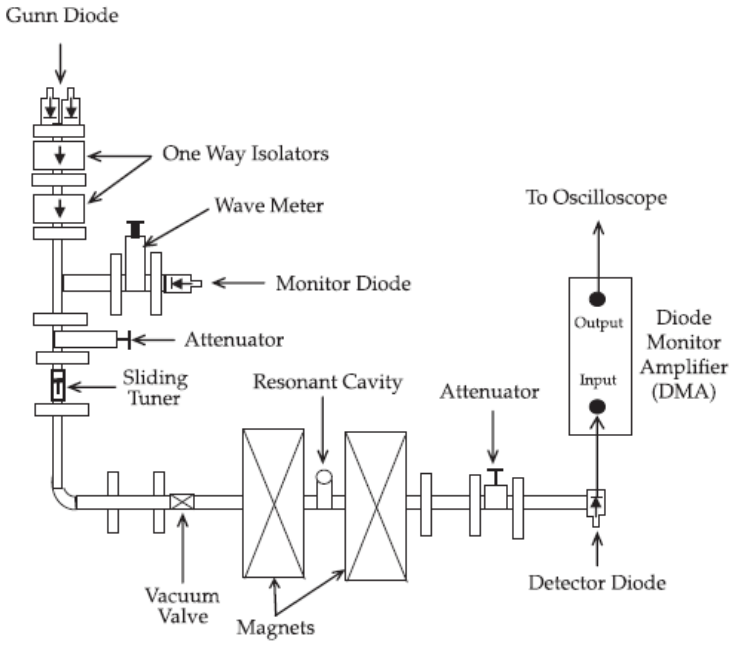

Figure 4: The initial apparatus setup

The magnet consisted of two sets of coils, the main coils, which are driven by the magnet power supply and used to provide a static magnetic field, plus a set of modulation coils, which provide a small oscillatory magnetic field of frequency 50Hz. A 50Hz voltage was used to drive the x plates of a double beam oscilloscope so that the horizontal sweep of the oscilloscope represented the oscillation to and fro of the field about the central value B. The signals from the EPR detector diode and the NMR probe were then displayed on the Y channels of the oscilloscope simultaneously and the static field B could be adjusted to bring both signals into the centre of the oscilloscope screen.

Unfortunately the signal we see is quite poor and noisy and so the signal recovery technique is required. The method we used to recover the signals from noise was to modulate the required measurements at a frequency which were in a less noisy part of the spectrum of the detection system. In this case we achieved this by modulating the local magnetic field at the sample inside the cavity by using a single loop of wire driven by a 115kHz oscillator. We then swept the magnetic field backwards and forwards rapidly through the EPR transition but within the line-width so that we can plot each point of the line shape.

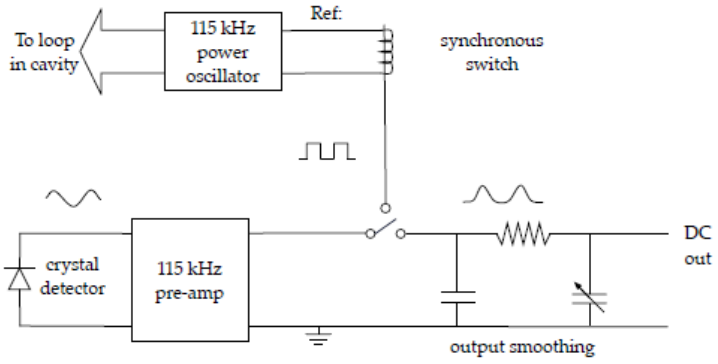

Figure 5: The signal recovery setup

After this the signal from the microwave diode, transmitted to a phase sensitive detector, was fed to a pre-amp tuned to 115kHz achieving some signal to noise improvement by filtering. Then the signal is further amplified to a suitable level to a transistor switch with the switch being turned on and off at the same rate as the modulated measurement. Hence, only signals that are the same frequency and phase coherent pass through, while other signals are attenuated. By modulating up to 115kHz low frequency noise is eliminated, but the shape of the NMR signal is unaffected as this frequency is slower than the proton relaxation time.

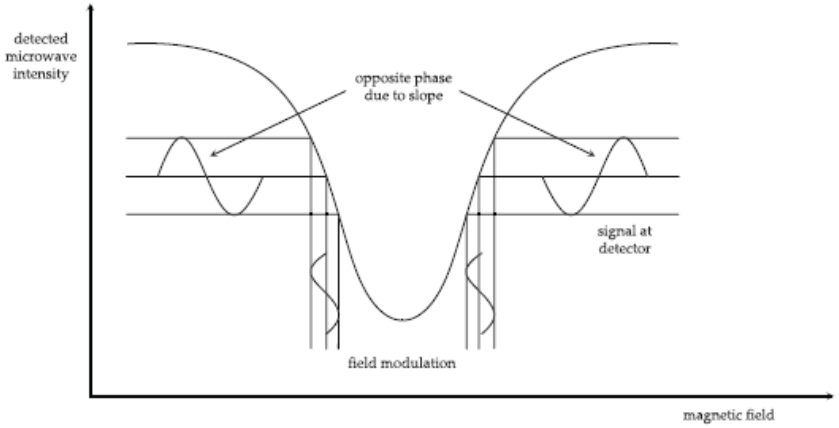

Figure 6: Pictorial representation of the process of phase sensitive

In this way, by applying a small 50 kHz modulation signal to the voltage tuning of the Gunn diode, an error signal is produced to lock the microwave frequency to the cavity resonance frequency. This produces a much steadier signal when you come to sweep the magnetic field.

While measuring the EPR signal we measured the applied magnetic field using a Hall probe. The data from the Hall probe was fed into the PC data acquisition unit and converted, by the provided software, into a magnetic field reading using the linear relationship between applied magnetic field and Hall voltage

$$B = aV + b \tag{6}$$

where a and b are constants. This relationship can be seen in figure 7 where the Hall voltage and applied magnetic field, estimated using the Hall voltage, have been plotted.

Calibration was necessary to determine these constants. To do this known values of the magnetic field needed to be applied to the Hall probe and the corresponding output reading recorded. These constants were initially determined by calibrating against the EPR signal of 1,1 Diphenyl-2-picryl-hydrazyl (DPPH). DPPH has a well-defined g-factor, giving a resonance at a particular value of magnetic field strength, which we independently measured using the NMR probe via the method previously described and compared with the Hall probe reading to determine the constants.

In general, the Hall voltage is not a linear function of B and is also a function of temperature, with nonlinearity coming from many sources such as the material's properties or geometrical factors. Over the range of field values we used, these nonlinearities typically produce a very small error and were thus neglected.

In principle this procedure should be repeated quite often to avoid problems with offset drifts However, during our experiment the Hall probe was calibrated once, before measurements were taken, and this would have incurred error in the magnetic field we measured.

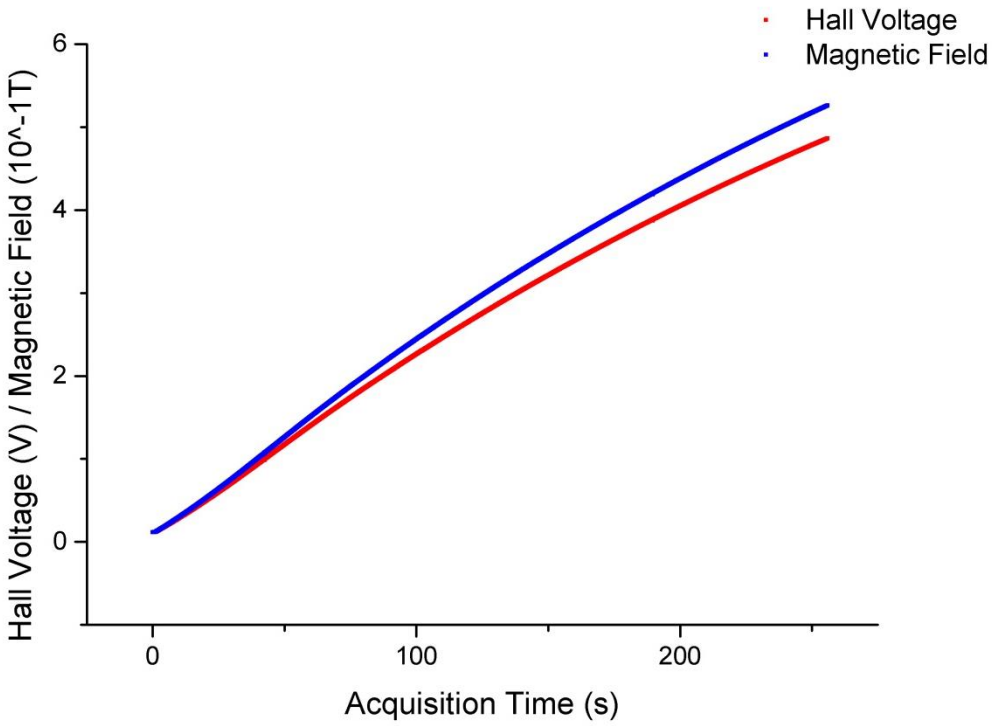

Figure 7: Measured Hall voltage and applied magnetic field strength estimate for $\phi = 0°$ on an upsweep

To record the EPR signal we used a PC data acquisition unit to slowly ramp the current to the magnet, while also measuring the monitor diode voltage and the Hall voltage detected by the Hall probe. The current was swept between a base value and a higher value over a set adjustable period. Using this technique allowed data to be collected more quickly and accurately.

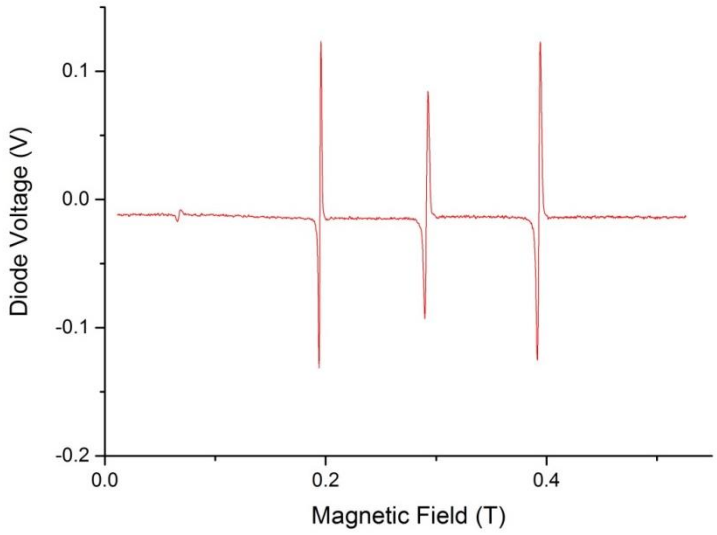

Figure 8: Observed EPR spectrum for $\phi = 180°$ on an upsweep

We measured the positions of the upper and lower peak for each resonance on the observed EPR spectrum as shown in figure 8 for both the upsweep and downsweep of the magnetic field using the PC data acquisition software. The process was repeated with the sample rotated by 5° in the apparatus 37 times to get data for angles from 0° to 180°.

5 Results

The final measured results are displayed in the table in figure 12 and plotted in figure 9. In the table each resonance is labelled from 1-4 in accordance with how the peaks were ordered in the observed EPR spectrum, an example of which is shown in figure 8 for $\phi = (180 \pm 2.5)°$. The final table of results was generated using the raw data which has been presented in appendix C for completeness.

A colour map is displayed in figure 10 showing the resonance field on an upsweep along with the associated diode voltage at each resonance which is related to the intensity of the transition. It is immediately noticeable that the lower curve is not visible since the associated transition is so weak, which can also be seen in figure 8. This is likely due to the low transition probability associated with this transition.

In addition to this several plots of the resonance field for various angles were computed using the program described in appendix A and compared with our measurements. A theoretical plot for $\theta = 67.0°$ is shown in figure 11 to demonstrate the 90° symmetry of the resonance field, which we expected due to the trigonal symmetry of the $\alpha - Al_2O_3$ lattice. From this we can also see that our measurements are offset by an orientation angle of either 35° or 145° (two possible values due to the symmetry of the resonance field) and this has been accounted for in the following plots comparing experimental and theoretical results in figures 15-17.

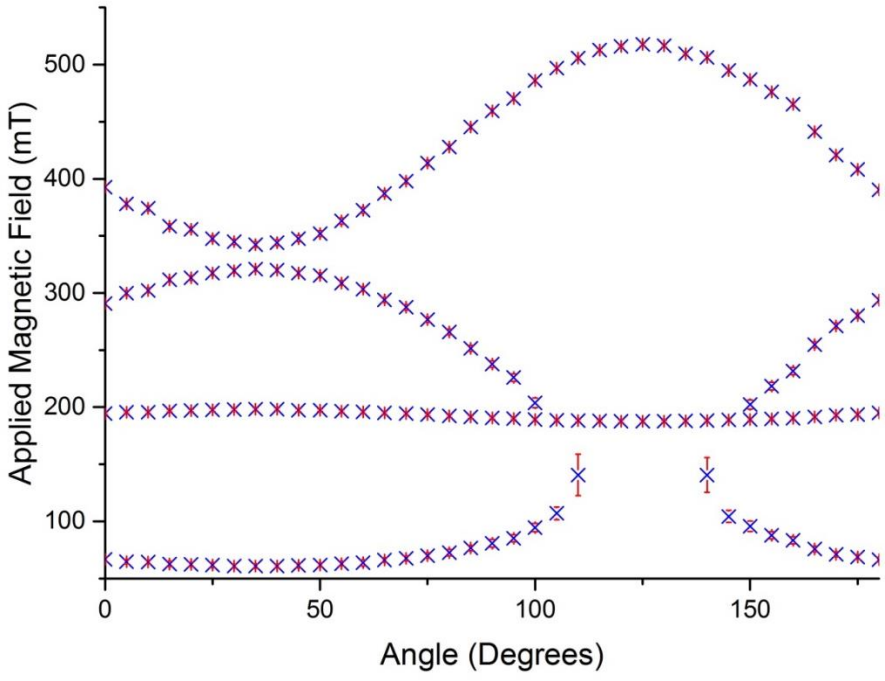

Figure 9: Plot of measured results and associated errors

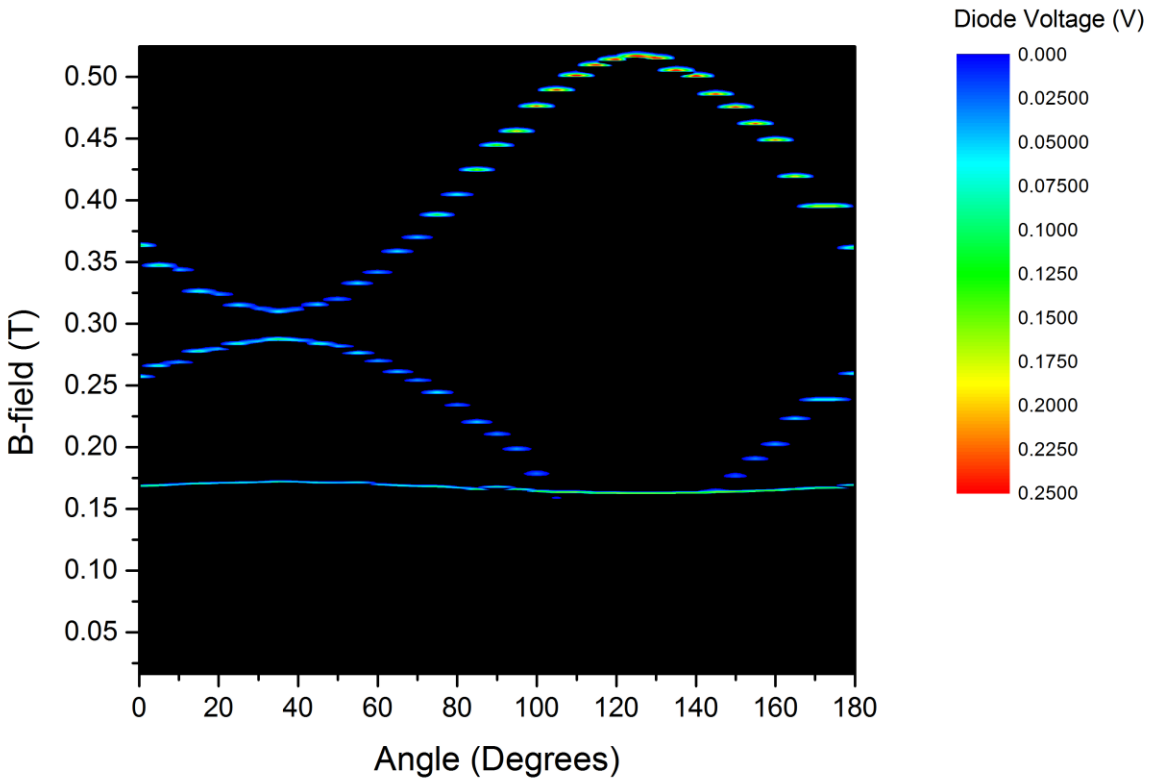

Figure 10: Colour map taken directly from our measured values on the upsweep.

The greater the diode voltage the greater the intensity of the observed peak.

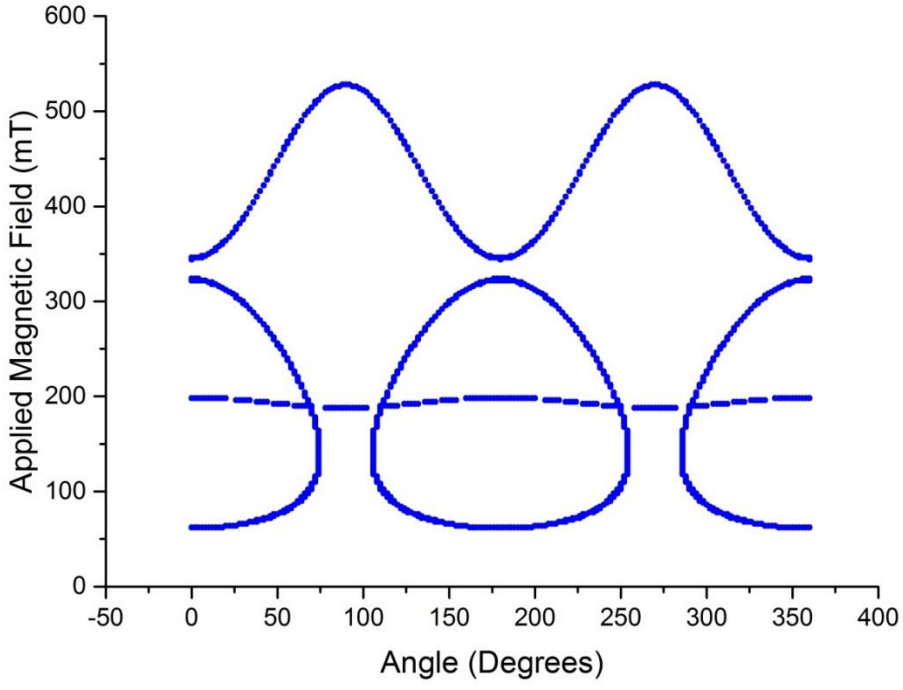

Figure 11: Theoretical plot of the resonance field for $\theta = 67.0^{\circ}$

Angle	Average Magnetic Field /mT							
	Resonance 1	Error	Resonance 2	Error	Resonance 3	Error	Resonance 4	Error
0	66.85	2.03	194.48	1.24	290.76	2.05	392.62	1.90
5	64.80	1.94	195.46	1.25	299.98	2.10	378.02	2.06
10	64.42	1.49	195.66	1.32	302.29	2.06	374.31	2.18
15	62.76	2.29	196.80	1.24	311.63	1.93	358.46	2.27
20	62.41	1.91	197.05	1.36	313.29	2.06	355.87	2.16
25	61.79	2.16	197.55	1.38	317.61	1.88	347.66	2.33
30	60.93	1.66	197.88	1.32	319.52	1.94	344.87	2.42
35	60.85	1.97	198.07	1.37	321.02	2.02	342.43	2.36
40	60.78	1.59	198.14	1.32	320.20	1.94	344.16	2.43
45	61.35	1.99	197.38	1.32	317.52	1.99	347.76	2.61
50	61.83	1.79	197.47	1.29	315.53	1.96	351.95	2.49
55	63.00	2.03	196.39	1.31	308.83	2.03	363.01	2.54
60	63.72	2.61	195.94	1.31	303.56	2.05	372.55	2.44
65	66.19	1.97	194.98	1.18	294.04	2.22	387.23	2.52
70	67.59	2.12	194.29	1.29	287.52	2.35	398.09	2.21
75	70.10	2.37	193.41	1.28	276.69	2.36	413.93	2.31
80	72.53	2.73	192.42	1.39	265.90	2.49	427.99	2.15
85	76.59	2.44	191.56	1.31	251.49	2.58	445.46	1.94
90	80.94	3.37	190.70	1.21	237.72	2.92	459.57	1.88
95	85.11	3.02	190.10	1.24	225.88	3.20	470.25	1.67
100	94.64	3.71	189.26	1.31	203.78	4.16	486.00	1.49
105	107.04	5.54	188.67	1.22			496.81	1.46
110	140.65	18.24	188.15	1.33			505.76	1.38
115			187.82	1.26			512.66	1.34
120			187.69	1.25			516.11	1.28
125			187.61	1.24			517.75	1.32
130			187.61	1.12			516.58	1.34
135			187.99	1.22			509.61	1.38
140	140.67	15.19	188.25	1.25			506.18	1.40
145	104.37	5.33	188.79	1.23			494.80	1.44
150	95.84	4.56	189.15	1.25	202.23	4.00	486.87	1.46
155	87.97	3.06	189.84	1.22	218.49	3.36	476.17	1.49
160	83.36	3.02	190.44	1.33	231.67	3.03	465.19	1.51
165	75.81	2.53	191.57	1.32	254.67	2.50	441.33	1.65
170	71.24	2.22	192.82	1.29	271.32	2.37	420.83	1.72
175	68.92	1.98	193.53	1.26	280.41	2.20	408.15	1.90
180	66.53	2.01	195.11	2.00	293.83	2.15	390.28	2.00

Figure 12: Table of final measured results with associated errors. Each observed resonance is labelled 1-4 going left to right on the EPR spectrum

Furthermore two sample plots of the energy levels of the Cr^{3+} ion versus applied magnetic field are shown in figures 13 and 14 for orientation angles $\phi = 0^{\circ}$ and $\phi = 90^{\circ}$. These demonstrate the broad features of the energy levels as the orientation angle is varied through 90° in that we go from a situation in which we have four resonances due to the energy levels having the appropriate spacing to a situation in which we have only two resonances, which is also what we see in figure 10. We also see that the sinusoidal pattern at high field observed in figure 10 is due to a transition between energy levels 3 and 4, the looped patterns are due to transitions between energy levels 2 and 3 and the almost linear pattern is due to a transition between levels 1 and 2.

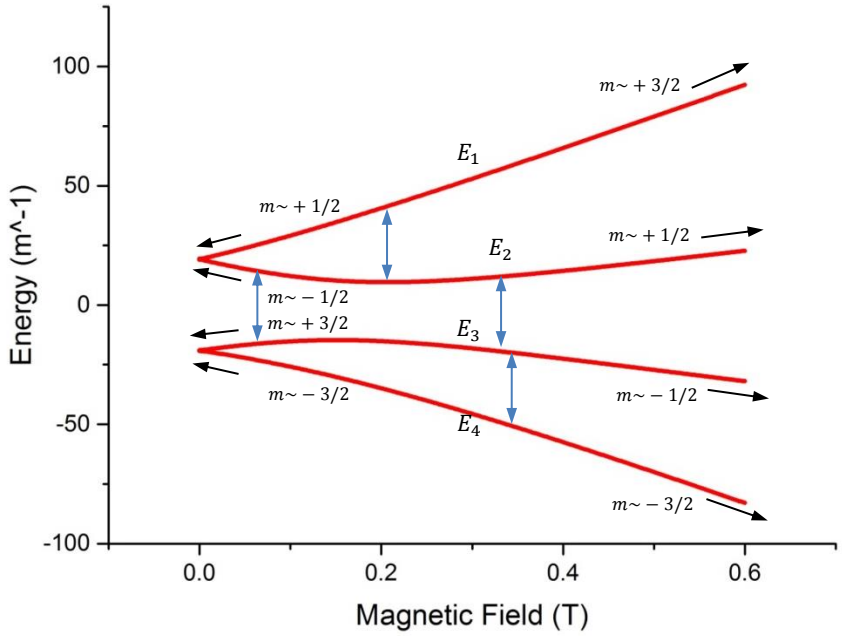

Figure 13: Plot of the energy levels for $\theta = 67.0°, \phi = 0^{\circ}$ where the blue lines refer to the transition energy

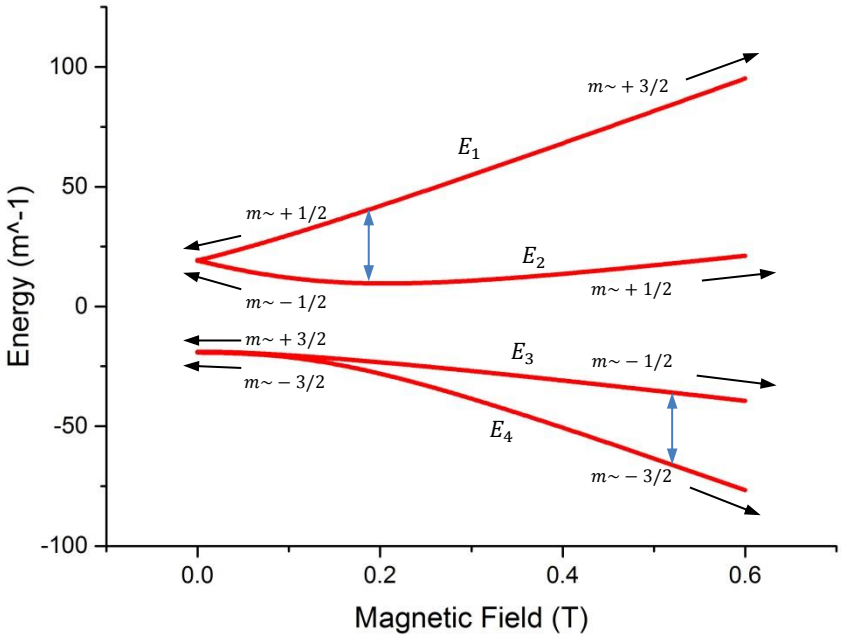

Figure 14: Plot of the energy levels for $\theta = 67.0°, \phi = 0^{\circ}$ where the blue lines refer to the transition energy

The experimental data closely matched the theoretical plot but there are some noticeable differences, namely that the theoretical plot gives results that are consistently about 11mT higher in value than our experimental results at $\theta \simeq 270^{\circ}$. However, it is still clear that the best fit angle of inclination to the plane of the magnetic field is one that lies within the range $66.0 < \theta < 67.0$ or $\theta = 66.5 \pm 0.5$.

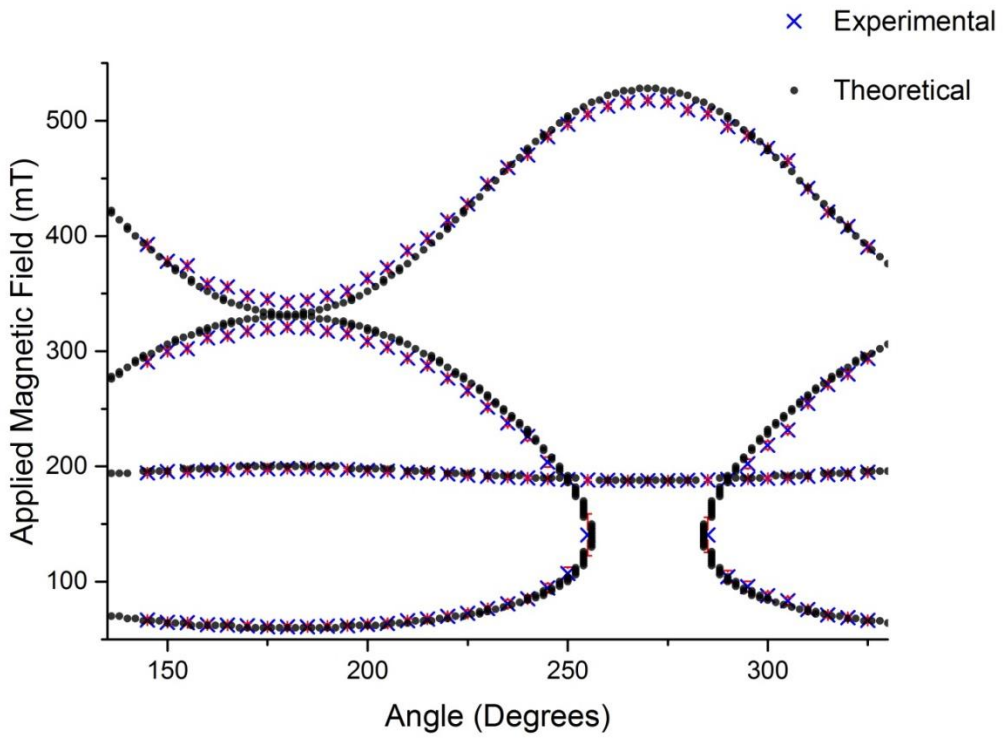

Figure 15: Measured results with theoretical results for $\theta = 66.0^{\circ}$ overlaid

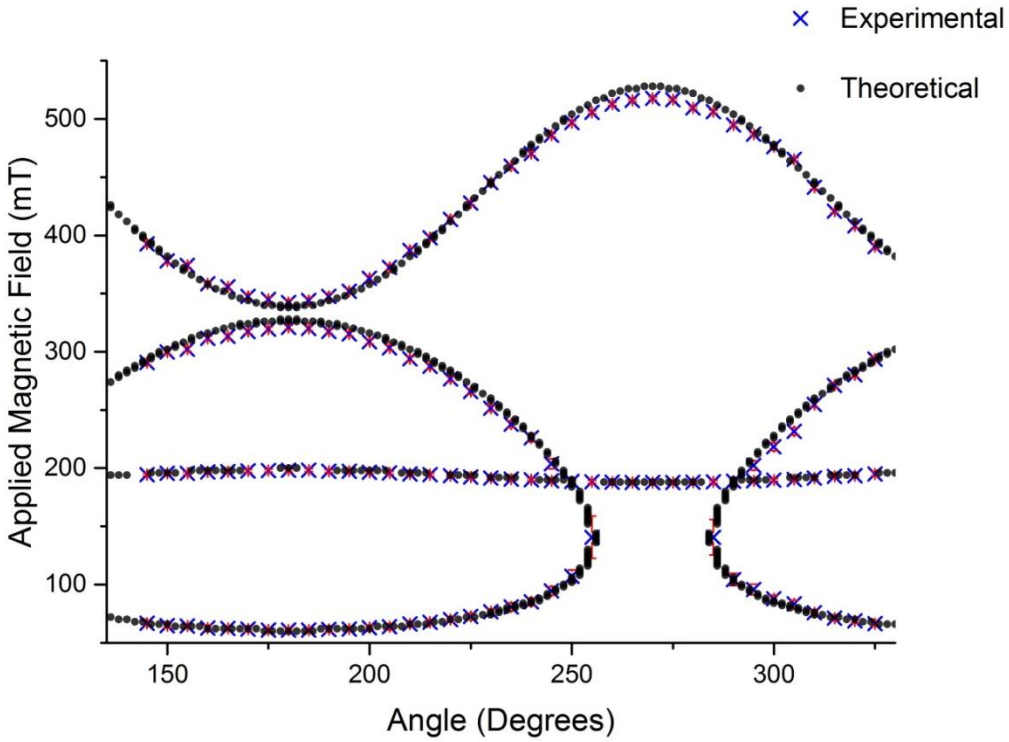

Figure 16: Measured results with theoretical results for $\theta = 66.5^{\circ}$ overlaid

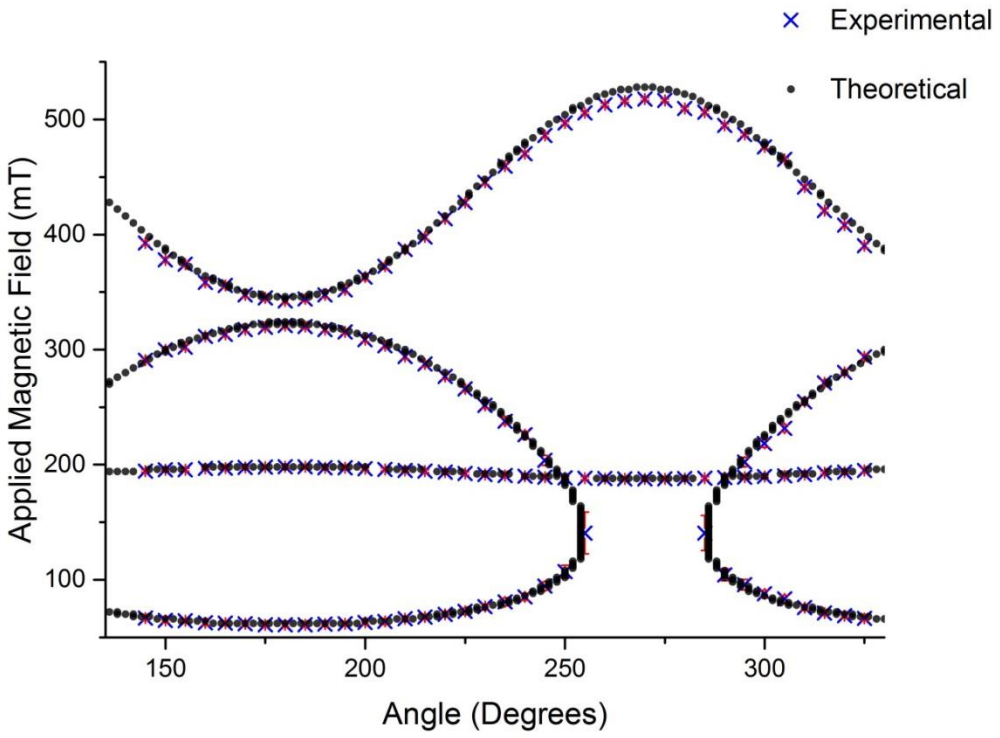

Figure 17: Measured results with theoretical results for $\theta = 67.0^\circ$ overlaid

6 Conclusion

The resonance spectrum of the Cr^{3+} ion seems to be generally described by the Hamiltonian (4). Comparing our measured results with the theoretical plots, numerically computed via the program in appendix A, we can conclude that the crystallographic axis of our ruby sample was tilted at an angle of $\theta = (66.5 \pm 1)^\circ$ to the plane defined by the applied magnetic field. At this angle our results are broadly consistent with the theoretical model.

The basic form for the energy levels of our system at this angle were determined and plotted for limiting cases. Which energy level each resonance we observed corresponded to was determined and we found the sinusoidal wave corresponded to transitions between levels 3 and 4, the looped patterns due to transitions between levels 2 and 3, and the slowly varying line corresponded to transitions between levels 1 and 2 with reference to the terminology used in figures 13 and 14.

There is, however, a significant discrepancy between our measured and calculated values of the resonance field since the peak of the theoretical plot at about 270° is always slightly higher than that of our measured plot for all angles and this deviation doesn't fall within our estimated error bounds.

This could be due to the fact that our theoretical model contains several simplifying assumptions:

- We have not accounted for the anisotropic nature of the g-factor, but instead assumed g to be a scalar quantity
- We have used values of g and D derived Collins and Morrison[2] which we expect to be close to those of our own ruby sample but may be slightly different from the actual values, incurring an error in our theoretical model

- Higher order terms of the spin operators have been ignored in our Hamiltonian which could generate a correction of sorts to our model

This could, therefore, potentially be resolved by using a better model that takes into account the anisotropy of the g-factor in our ruby crystal as well as higher order spin operator terms in our spin Hamiltonian.

Furthermore, this systematic discrepancy could be due to errors in the calibration used in Hall probe. An error, for example, in the value of a in equation (6) could lead to all measured values of applied magnetic field to be slightly offset and would produce a noticeable deviation at high magnetic fields where discrepancies in a would be more greatly enhanced. This systematic error could be accounted for by performing the calibration more often and with a greater range of samples to calibrate against.

Values of g and D which more accurately describe the sample we used could be obtained by first independently measuring the orientation of the crystal axis with respect to the externally applied magnetic field. With this knowledge and treating g and D as fit parameters we can numerically determine which values give us the best agreement between theoretical and experimental measurements.

Lastly, in regards to the limitations of our procedure, we noted the extremely low intensity resonance for the lower level 2-3 transition which could not be accounted for using our program since it only described the energy levels of the Cr^{3+} ion and computed the resonance field. It is believed that, through further work, the intensity of absorption could be described by determining the transmission probabilities for each resonance. This could, in principal, be achieved numerically using the same theoretical model for the Hamiltonian of the system that we previously used to determine the energy levels.

References

[1] E. O. Schulz-Dubois, Bell Syst. Tech. J. 38, 271 (1959)

[2] L. A. Collins, M. A. Morrison, P. L. Donoho, AJP 42, 560 (1974)

[3] Geusic, J. E., Phys. Rev., 102, June 15, 1956, p. 1252; also Ph. D. dissertation, Ohio State Univ. (1958)

[4] Bleaney, B. and Stevens, K. W. H., Paramagnetic Resonance, Rep. Prog. Phys., 16, 1953, p. 107

[5] Nicholas, R. J., SS12 Practical Script, Oxford Physics (2011)

Acknowledgments

The author wishes to express his appreciation to David Buckley for his helpful discussions and the Oxford Physics Practical course for providing the necessary equipment.

Appendix A Source Code

The source code used to compute the theoretical resonance field for the Cr^{3+} ion in the ruby crystal for an applied magnetic field within the range $0\text{T} < B < 0.6\text{T}$, orientation angle within the range $0° < \theta < 360°$and a fixed azimuthal tilt angle which is manually entered:

```
/*************************************************************************
*  SS12 Paramagnetic Resonance – Aravinth Kulanthaivelu 07/02/2015
*  A program designed to compute resonance fiel for the trivalent chromium ion
*  in an applied magnetic field for a range of orientation angles relative
*  to the plane of the field, given a frequency, g-factor, D constant and
*  azimuthal tilt angle
*************************************************************************/

#include <math.h>
#include <stdio.h>
#include <stdlib.h>


/*Function evaluate the secular equation for a given value of x1*/

double f1(double x1, double B, double a, double t)
{
	double D = 19.155;
	double mu = 46.68643714;
	double g = 1.98535;

	return (pow(x1, 4) - (2.0*D*D + (5.0*(g*mu*B)*(g*mu*B)) / 2.0)*(x1*x1)
		+ (2.0*D*(g*mu*B)*(g*mu*B))*(3.0*(cos((M_PI)*t / 180.0)
		*cos((M_PI)*t / 180.0))*(cos(a)*cos(a)) - 1.0)*x1 +
		((D*g*mu*B)*(D*g*mu*B))*(1.0 - 6.0*(cos((M_PI)*t / 180.0)*
		cos((M_PI)*t / 180.0))*(cos(a)*cos(a))) / 2.0
		+ 9.0*(pow((g*mu*B), 4.0)) / 16.0 + pow(D, 4.0));
}


/*Function evaluate the derivative of the secular equation for a given value
of x1*/

double f1_prime(double x1, double B, double a, double t)
{
	double D = 19.155;
	double mu = 46.68643714;
	double g = 1.98535;

	return (4.0*(x1*x1) - (4.0*D*D + 5.0*(g*mu*B)*(g*mu*B))*x1
		+ 2.0*D*((g*mu*B)*(g*mu*B))*(3.0*(cos((M_PI)*t / 180.0)*
		cos((M_PI)*t / 180.0)*cos(a)*cos(a)) - 1.0));
}


/*Function identical to f1 but with (x2-x1) factored out to avoid convergence
onto the same value that the previous iteration returns*/

double f2(double x2, double x1, double B, double a, double t)
{
	return (f1(x2, B, a, t) / (x2 - x1));
}


/*Function that evaluates the derivative of f2 for a given value of x2*/

double f2_prime(double x2, double x1, double B, double a, double t)
```

```
{
	return (f1_prime(x2, B, a, t) / (x2 - x1) -
		f1(x2, B, a, t) / ((x2 - x1)*(x2 - x1)));
}


/*Function that evaluates the solution to the resulting quadratic equation
using the quadratic formula with the positive sign taken for
the discriminant*/

double f3(double x1, double x2, double B, double a, double t)
{
	double D = 19.155;
	double mu = 46.68643714;
	double g = 1.98535;
	double p;
	p = -(2.0*D*D + (5.0*(g*mu*B)*(g*mu*B)) / 2.0);
	return((0.5)*(-(x1 + x2) + sqrt((x2 + x1)*(x2 + x1) -
		4.0*(x2*x2 + x2*x1 + x1*x1 + p))));
}


/*Function that evaluates the solution to the resulting quadratic equation
using the quadratic formula with the negative sign taken for
the discriminant*/

double f4(double x1, double x2, double B, double a, double t)
{
	double D = 19.155;
	double mu = 46.68643714;
	double g = 1.98535;
	double p;
	p = -(2.0*D*D + (5.0*(g*mu*B)*(g*mu*B)) / 2.0);
	return((0.5)*(-(x1 + x2) - sqrt((x2 + x1)*(x2 + x1) -
		4.0*(x2*x2 + x2*x1 + x1*x1 + p))));
}


int main()
{
	/*Variables are defined; Values of D and g are taken to be constant
	and defined here in units of wavenumbers */

	int i, j, k;
	double E[361][101][4];
	double D = 19.155;
	double mu = 46.68643714;
	double g = 1.98535;
	double B, a, t;
	double x1, x2, x3, x4;
	double T = 30.8;
	double q1, q2, q3, q4;

	FILE *fout;

	if ((fout = fopen("SS12.txt", "w")) == NULL)
	{
		printf("Cannot open %s\n", "SS12.txt");
		exit(EXIT_FAILURE);
	}

	printf("Enter a value for the crystal deviation angle t\n");
	scanf("%lf", &t);
```

```
/*The secular equation is solved for a range of values of orientation angle
and magnetic field*/

for (i = 0; i<101; i++)
{
	for (j = 0; j<361; j++)
	{
		B = (0.006)*(double)i;

		a = ((M_PI)*(double)j) / 180.0;


		/*The starting point of the Newton-Raphson procedure is taken to be
		the inflection point of our quartic secular equation*/

		x1 = sqrt((2.0*D*D + (5.0*(g*mu*B)*(g*mu*B) / 2.0)) / 6.0);
		x2 = -sqrt((2.0*D*D + (5.0*(g*mu*B)*(g*mu*B) / 2.0)) / 6.0);

		for (k = 0; k<100; k++) /*The Newton-Raphson iteration run for x1*/
		{
			x1 = x1 - (f1(x1, B, a, t) / f1_prime(x1, B, a, t));

		}

		for (k = 0; k<100; k++) /*The Newton-Raphson iteration run for x2*/
		{
			x2 = x2 - (f2(x2, x1, B, a, t) / f2_prime(x2, x1, B, a, t));

		}

		x3 = f3(x1, x2, B, a, t); /*x3 is found by solving the resulting
					  quadratic*/

		x4 = f4(x1, x2, B, a, t); /*x4 is found from the other solution of the
					  resulting quadratic*/

		/*The values of angle, magnetic field and resonance are
		stored in the array*/

		E[j][i][0] = x1;
		E[j][i][1] = x2;
		E[j][i][2] = x3;
		E[j][i][3] = x4;
	}
}

for (i = 0; i<101; i++)
{
	for (j = 0; j<361; j++)
	{
		B = (0.006)*(double)i;

		/*The transition energy between energy levels satisfying the
		selection rules is computed*/

		q1 = fabs(E[j][i][0] - E[j][i][1]);

		q2 = fabs(E[j][i][0] - E[j][i][2]);

		q3 = fabs(E[j][i][1] - E[j][i][3]);

		q4 = fabs(E[j][i][2] - E[j][i][1]);

		/*If our computed transition energy matches the theoretical
		interaction energy the magnetic field and orientation
```

```
                        angle of the resonance is printed*/

                        if (fabs(q1 - T)<0.12)
                        {
                               fprintf(fout, "%d\t %f\n", j, B);
                        }

                        if (fabs(q2 - T)<0.4)
                        {
                               fprintf(fout, "%d\t %f\n", j, B);
                        }

                        if (fabs(q3 - T)<0.175)
                        {
                               fprintf(fout, "%d\t %f\n", j, B);
                        }

                        if (fabs(q4 - T)<0.3)
                        {
                               fprintf(fout, "%d\t %f\n", j, B);
                        }

                }
        }

}
    exit(0); }
```

Appendix B Derivation of the Spin Hamiltonian and Eigenvalue Equation

The four spin states of the Cr^{3+} ion in Al_2O_3 are eigenstates of the operators S^2 and S_z which have the usual definitions, and so they are characterised by the quantum numbers $S = \frac{3}{2}, m = \frac{3}{2}, \frac{1}{2}, -\frac{1}{2}, -\frac{3}{2}$. It is important to note that these operators are defined with respect to the crystallographic axis of our sample such that S_z is aligned with this crystal axis.

In the case of zero applied field, the crystal field causes a small splitting in the energy levels corresponding to $m = \pm\frac{1}{2}$ and $m = \pm\frac{3}{2}$. This splitting into two doublets is much smaller than the separation of the orbital levels and is called the zero field splitting owing to the fact that it is a splitting of the ground state spin multiplet and occurs in the absence of an applied magnetic field. Once a magnetic field is applied we get a normal Zeeman splitting of the two doublets and the ground state spin multiplet is split into four states with different energies.

The crystal field, which splits the four states into two doublets, can be described by

$$H_C = -D\left(S_z^2 - \frac{5}{4}\right) \tag{B.1}$$

where D is a constant characteristic of the splitting.
In the case of zero field splitting this gives

$$E_C = -D\left(m^2 - \frac{5}{4}\right) = \begin{cases} +D, & m = \pm 1/2 \\ -D, & m = \pm 3/2 \end{cases} \tag{B.2}$$

giving us our two energy levels.

Ignoring for the moment the zero field splitting, the effect of the magnetic field, which generates the normal Zeeman splitting of the four energy levels can be described by the usual Zeeman interaction Hamiltonian

$$H_Z = g\mu_B \mathbf{B} \cdot \mathbf{S} \tag{B.3}$$

where, in general, g would be a tensor, having different values depending upon whether the applied field is parallel to the crystal axis or perpendicular to it. Here we assume g to be a scalar and so the Zeeman Hamiltonian leads to energy levels given by (2). However the choice of the z axis isn't arbitrary but must coincide with the crystallographic axis shown in figure B1 on account of the rotational symmetry of the crystal field.

The two terms (B.1) and (B.3) describing the effects of the magnetic field and the crystalline electric field can be added to produce a resultant spin Hamiltonian which provides a complete description of all aspects of the static and dynamic behaviour of the four spin levels under the application of both static and time-dependent magnetic fields.

$$H = g\mu_B \mathbf{B} \cdot \mathbf{S}' - D\left(S_z^2 - \frac{5}{4}\right) \tag{B.4}$$

In our experiment we kept the magnetic field constant and altered the orientation of the crystal axis and thus the axis relative to which our spin operator is defined. Thus we can model the situation with a magnetic field acting in the z with the crystal axis rotating about the x axis. This corresponds to a situation in figure B1 with $\phi = 0$.

$$\mathbf{S}' = \mathrm{R}_y(-\theta)\mathbf{S} = \begin{pmatrix} \cos\theta & 0 & -\sin\theta \\ 0 & 1 & 0 \\ \sin\theta & 0 & \cos\theta \end{pmatrix} \begin{pmatrix} S_x \\ S_y \\ S_z \end{pmatrix} = \begin{pmatrix} S_x\cos\theta - S_z\sin\theta \\ S_y \\ S_x\sin\theta + S_z\cos\theta \end{pmatrix} \tag{B.5}$$

This gives the representation of the spin vector with the crystal axis tilted by an angle θ to the axis defined by the magnetic field. Equivalently we can think of it as the spin vector at an angle theta to the z direction whilst in the x-z plane.

We can model the process of rotating the crystallographic axis in the plane define by the magnetic field by considering the rotation of our effective spin vector about the x axis by an angle ϕ, whilst maintaining the angle of inclination from the magnetic field vector by an angle θ.

$$\begin{aligned} \mathrm{R}_x(\phi) &= \begin{pmatrix} 1 & 0 & 0 \\ 0 & \cos\phi & -\sin\phi \\ 0 & \sin\phi & \cos\phi \end{pmatrix} \begin{pmatrix} S_x\cos\theta - S_z\sin\theta \\ S_y \\ S_x\sin\theta + S_z\cos\theta \end{pmatrix} \\ &= \begin{pmatrix} S_x\cos\theta - S_z\sin\theta \\ S_y\cos\phi - S_x\sin\theta\sin\phi + S_z\cos\theta\sin\phi \\ S_y\sin\phi + S_x\sin\theta\cos\phi + S_z\cos\theta\cos\phi \end{pmatrix} \end{aligned} \tag{B.6}$$

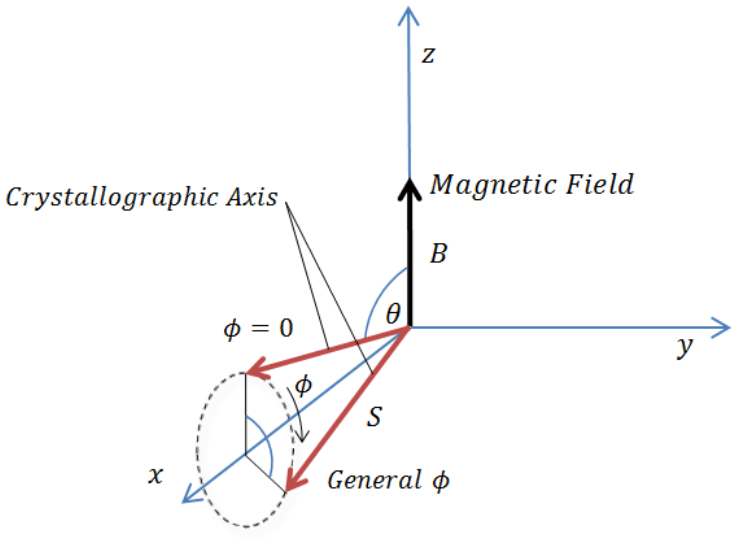

Figure B1: Effective vector model representation of rotating the sample in our experiment

For $S = 3/2$ states in the representation $|i\rangle = |s, m_i\rangle$, the corresponding spin operators are

$$S_x = \begin{pmatrix} 0 & \sqrt{3}/2 & 0 & 0 \\ \sqrt{3}/2 & 0 & 1 & 0 \\ 0 & 1 & 0 & \sqrt{3}/2 \\ 0 & 0 & \sqrt{3}/2 & 0 \end{pmatrix}, \quad S_y = \begin{pmatrix} 0 & -i\sqrt{3}/2 & 0 & 0 \\ i\sqrt{3}/2 & 0 & -i & 0 \\ 0 & i & 0 & -i\sqrt{3}/2 \\ 0 & 0 & i\sqrt{3}/2 & 0 \end{pmatrix} \tag{B.7}$$

$$S_z = \begin{pmatrix} 3/2 & 0 & 0 & 0 \\ 0 & 1/2 & 0 & 0 \\ 0 & 0 & -1/2 & 0 \\ 0 & 0 & 0 & -3/2 \end{pmatrix}$$

Substituting these expressions into (B.4) we get the Hamiltonian matrix

$$H = \begin{pmatrix} \frac{3}{2}C - D & \sqrt{3}S^*/2 & 0 & 0 \\ \sqrt{3}S/2 & \frac{1}{2}C + D & S^* & 0 \\ 0 & S & -\frac{1}{2}C + D & \sqrt{3}S^*/2 \\ 0 & 0 & \sqrt{3}S/2 & -\frac{3}{2}C - D \end{pmatrix} \tag{B.8}$$

$$C = g\mu_B B\cos\theta\cos\phi\,, \qquad S = g\mu_B B(\sin\theta\cos\phi + i\sin\phi)$$

For a state $\Phi_{\mathrm{n}} = A_{n1}|1\rangle + A_{n2}|2\rangle + A_{n3}|3\rangle + A_{n4}|4\rangle$ the time-independent Schrodinger equation becomes

$$\begin{pmatrix} 3C/2 - D - E_n & \sqrt{3}S/2 & 0 & 0 \\ \sqrt{3}S/2 & C/2 + D - E_n & S & 0 \\ 0 & S & -C/2 + D - E_n & \sqrt{3}S/2 \\ 0 & 0 & \sqrt{3}S/2 & -3C/2 - D - E_n \end{pmatrix} \begin{pmatrix} A_{n1} \\ A_{n2} \\ A_{n3} \\ A_{n4} \end{pmatrix} = \begin{pmatrix} 0 \\ 0 \\ 0 \\ 0 \end{pmatrix} \tag{B.9}$$

Diagonalising this matrix we get the secular equation for each of the four energy levels as a function of θ and ϕ

$$\begin{aligned} E_n^4 - E_n^2\left[2D^2 + \frac{5}{2}(g\mu_B B)^2\right] + 2DE_n(g\mu_b B)^2(3\cos^2\theta\cos^2\phi - 1) + D^4 \\ + \frac{9}{16}(g\mu_B B)^4 + \frac{1}{2}D^2(g\mu_B B)^2(1 - 6\cos^2\theta\cos^2\phi) = 0 \end{aligned} \tag{B.10}$$

Appendix C Full Table of Acquired Results

	Upsweep Magnetic Field/ mT															
	Resonance 1				Resonance 2				Resonance 3				Resonance 4			
Angle	Upper	Lower	Average	Error	Upper	Lower	Average	Error	Upper	Lower	Average	Error	Upper	Lower	Average	Error
0	69.07	66.00	67.54	1.53	195.67	194.03	194.85	0.82	292.53	289.67	291.10	1.43	394.27	391.59	392.93	1.34
5	66.82	63.96	65.39	1.43	196.75	195.11	195.93	0.82	301.84	298.93	300.38	1.46	379.81	376.93	378.37	1.44
10	65.70	63.58	64.64	1.06	196.87	195.22	196.05	0.83	304.10	301.25	302.67	1.43	376.19	373.22	374.70	1.49
15	65.06	61.72	63.39	1.67	198.03	196.38	197.20	0.82	313.32	310.52	311.92	1.40	360.33	357.15	358.74	1.59
20	64.14	61.98	63.06	1.08	198.50	196.63	197.57	0.93	315.23	312.37	313.80	1.43	357.77	354.74	356.26	1.51
25	63.77	60.71	62.24	1.53	198.86	197.02	197.94	0.92	319.30	316.70	318.00	1.30	349.68	346.44	348.06	1.62
30	62.80	59.98	61.39	1.41	199.24	197.42	198.33	0.91	321.14	318.60	319.87	1.27	346.92	343.60	345.26	1.66
35	62.66	59.80	61.23	1.43	199.40	197.75	198.57	0.83	322.85	320.04	321.44	1.41	344.39	341.15	342.77	1.62
40	62.73	60.58	61.66	1.07	199.54	197.72	198.63	0.91	321.89	319.28	320.59	1.31	346.21	342.92	344.57	1.65
45	63.25	60.44	61.85	1.40	198.75	196.87	197.81	0.94	319.26	316.50	317.88	1.38	349.95	346.28	348.11	1.84
50	63.50	60.89	62.19	1.31	198.58	196.94	197.76	0.82	317.28	314.67	315.98	1.31	354.06	350.63	352.34	1.71
55	64.88	62.30	63.59	1.29	197.74	195.85	196.79	0.95	310.61	307.79	309.20	1.41	365.12	361.58	363.35	1.77
60	65.50	63.11	64.31	1.19	197.23	195.38	196.31	0.93	305.42	302.56	303.99	1.43	374.70	371.13	372.92	1.78
65	67.60	65.23	66.41	1.18	196.08	194.46	195.27	0.81	295.93	292.81	294.37	1.56	389.36	385.89	387.62	1.73
70	70.06	66.43	68.25	1.81	195.58	193.76	194.67	0.91	289.61	286.26	287.93	1.68	400.00	396.97	398.49	1.52
75	72.22	69.12	70.67	1.55	194.72	192.92	193.82	0.90	278.79	275.39	277.09	1.70	415.84	412.53	414.18	1.66
80	74.57	71.23	72.90	1.67	193.75	191.96	192.85	0.90	268.06	264.60	266.33	1.73	429.77	426.86	428.32	1.45
85	78.58	75.12	76.85	1.73	192.91	191.07	191.99	0.92	253.77	250.06	251.92	1.85	447.14	444.48	445.81	1.33
90	84.26	78.89	81.57	2.69	191.83	190.24	191.04	0.79	240.10	235.91	238.00	2.10	461.11	458.49	459.80	1.31
95	87.76	83.53	85.64	2.11	191.30	189.66	190.48	0.82	228.51	224.04	226.27	2.23	471.73	469.34	470.54	1.19
100	97.85	92.19	95.02	2.83	190.58	188.75	189.67	0.92	207.06	201.81	204.43	2.63	487.28	485.28	486.28	1.00
105	111.68	103.99	107.84	3.85	189.87	188.24	189.05	0.81					498.06	496.09	497.07	0.98
110	153.88	129.52	141.70	12.18	189.51	187.69	188.60	0.91					507.02	505.12	506.07	0.95
115					189.09	187.45	188.27	0.82					513.81	512.04	512.93	0.89
120					188.91	187.30	188.10	0.80					517.26	515.49	516.37	0.88

125					188.81	187.23	188.02	0.79					518.97	517.09	518.03	0.94
130					188.74	187.12	187.93	0.81					517.83	515.94	516.89	0.94
135					189.18	187.55	188.36	0.81					510.86	508.96	509.91	0.95
140	152.83	131.41	142.12	10.71	189.50	187.86	188.68	0.82					507.49	505.52	506.51	0.99
145	108.65	100.58	104.62	4.03	190.01	188.36	189.19	0.83					496.13	494.15	495.14	0.99
150	99.84	92.53	96.18	3.66	190.42	188.77	189.59	0.83	205.35	200.00	202.68	2.67	488.17	486.15	487.16	1.01
155	90.19	86.28	88.24	1.95	191.02	189.40	190.21	0.81	221.25	216.71	218.98	2.27	477.52	475.46	476.49	1.03
160	85.94	81.93	83.94	2.00	191.68	190.09	190.89	0.79	234.26	230.04	232.15	2.11	466.53	464.45	465.49	1.04
165	77.94	74.24	76.09	1.85	192.95	191.11	192.03	0.92	256.74	253.28	255.01	1.73	442.86	440.48	441.67	1.19
170	72.88	70.47	71.67	1.21	193.99	192.40	193.19	0.79	273.45	270.02	271.73	1.72	422.30	419.96	421.13	1.17
175	70.78	67.86	69.32	1.46	194.82	193.22	194.02	0.80	282.40	279.26	280.83	1.57	409.82	407.12	408.47	1.35
180	68.56	65.88	67.22	1.34	197.57	194.31	195.94	1.63	294.43	291.33	292.88	1.55	391.99	389.24	390.61	1.37

	Downsweep Magnetic Field/ mT															
	Resonance 1				**Resonance 2**				**Resonance 3**				**Resonance 4**			
Angle	**Upper**	**Lower**	**Average**	**Error**	**Upper**	**Lower**	**Average**	**Error**	**Upper**	**Lower**	**Average**	**Error**	**Upper**	**Lower**	**Average**	**Error**
0	67.33	65.02	66.17	1.16	194.95	193.26	194.10	0.85	291.85	288.98	290.41	1.43	393.62	390.99	392.31	1.32
5	65.38	63.03	64.21	1.17	195.81	194.16	194.98	0.82	301.03	298.12	299.58	1.46	379.12	376.24	377.68	1.44
10	65.21	63.17	64.19	1.02	196.23	194.34	195.28	0.95	303.32	300.47	301.90	1.43	375.47	372.38	373.93	1.54
15	63.57	60.69	62.13	1.44	197.23	195.57	196.40	0.83	312.64	310.03	311.33	1.30	359.78	356.59	358.18	1.59
20	63.18	60.32	61.75	1.43	197.37	195.69	196.53	0.84	314.17	311.40	312.78	1.39	356.98	353.99	355.48	1.50
25	62.78	59.87	61.33	1.45	198.12	196.20	197.16	0.96	318.51	315.92	317.21	1.30	348.89	345.64	347.26	1.62
30	61.22	59.70	60.46	0.76	198.26	196.59	197.43	0.84	320.58	317.75	319.16	1.42	346.19	342.76	344.48	1.71
35	61.77	59.16	60.47	1.30	198.54	196.61	197.58	0.97	321.98	319.21	320.59	1.39	343.77	340.41	342.09	1.68
40	60.70	59.11	59.91	0.79	198.46	196.83	197.64	0.81	321.21	318.44	319.82	1.39	345.50	342.01	343.76	1.74
45	62.16	59.53	60.85	1.31	197.76	196.12	196.94	0.82	318.55	315.77	317.16	1.39	349.22	345.58	347.40	1.82

50	62.65	60.29	61.47	1.18	198.12	196.22	197.17	0.95	316.49	313.69	315.09	1.40	353.31	349.79	351.55	1.76
55	63.86	60.96	62.41	1.45	196.81	195.17	195.99	0.82	309.86	307.05	308.45	1.40	364.47	360.89	362.68	1.79
60	65.36	60.90	63.13	2.23	196.41	194.72	195.56	0.85	304.54	301.72	303.13	1.41	373.82	370.56	372.19	1.63
65	67.52	64.41	65.96	1.55	195.51	193.88	194.69	0.81	295.25	292.16	293.71	1.55	388.62	385.04	386.83	1.79
70	67.84	66.03	66.93	0.91	194.74	193.08	193.91	0.83	288.70	285.52	287.11	1.59	399.25	396.12	397.69	1.56
75	71.23	67.84	69.54	1.69	193.80	192.19	193.00	0.81	277.87	274.71	276.29	1.58	415.27	412.10	413.69	1.59
80	74.29	70.04	72.16	2.13	192.95	191.03	191.99	0.96	267.22	263.74	265.48	1.74	429.22	426.12	427.67	1.55
85	78.04	74.64	76.34	1.70	191.96	190.30	191.13	0.83	252.81	249.31	251.06	1.75	446.48	443.75	445.11	1.36
90	82.27	78.36	80.32	1.95	191.20	189.51	190.36	0.84	239.45	235.42	237.43	2.02	460.67	458.00	459.34	1.33
95	86.68	82.49	84.58	2.10	190.58	188.87	189.72	0.85	227.74	223.22	225.48	2.26	471.10	468.84	469.97	1.13
100	96.63	91.87	94.25	2.38	189.71	188.02	188.86	0.85	206.29	199.97	203.13	3.16	486.78	484.64	485.71	1.07
105	110.15	102.36	106.25	3.90	189.10	187.46	188.28	0.82					497.60	495.51	496.55	1.04
110	153.12	126.08	139.60	13.52	188.55	186.83	187.69	0.86					506.41	504.50	505.45	0.95
115					188.21	186.52	187.37	0.84					513.35	511.42	512.39	0.96
120					188.15	186.43	187.29	0.86					516.74	514.97	515.85	0.89
125					188.06	186.34	187.20	0.86					518.34	516.59	517.47	0.88
130					188.00	186.58	187.29	0.71					517.19	515.36	516.27	0.91
135					188.44	186.78	187.61	0.83					510.26	508.37	509.32	0.95
140	149.88	128.55	139.22	10.67	188.67	186.98	187.83	0.84					506.79	504.90	505.85	0.94
145	107.60	100.64	104.12	3.48	189.23	187.57	188.40	0.83					495.44	493.48	494.46	0.98
150	98.21	92.78	95.50	2.72	189.53	187.88	188.70	0.82	204.73	198.85	201.79	2.94	487.60	485.57	486.59	1.01
155	90.04	85.35	87.70	2.34	190.30	188.63	189.46	0.83	220.42	215.56	217.99	2.43	476.88	474.83	475.85	1.03
160	84.98	80.60	82.79	2.19	190.96	189.03	189.99	0.97	233.32	229.07	231.20	2.13	465.96	463.84	464.90	1.06
165	77.23	73.82	75.52	1.71	191.95	190.28	191.12	0.84	256.10	252.57	254.33	1.76	442.09	439.90	440.99	1.10
170	72.61	69.00	70.81	1.80	193.39	191.51	192.45	0.94	272.49	269.33	270.91	1.58	421.74	419.30	420.52	1.22
175	69.80	67.23	68.51	1.28	193.88	192.20	193.04	0.84	281.46	278.50	279.98	1.48	409.12	406.52	407.82	1.30
180	67.16	64.51	65.84	1.33	195.10	193.46	194.28	0.82	295.93	293.64	294.78	1.14	391.35	388.53	389.94	1.41

Each value in our table of final results was acquired by averaging over each observed peak on the upsweep and downsweep individually, in order to obtain an estimate for each absorption peak, and then by averaging corresponding upsweep and downsweep results to correct for the error associated with magnetic calibration. The errors were computed by estimating the error associated with averaging the upper and lower peaks to find the absorption peaks and the error associated with averaging over our upsweep and downsweep results before being added in quadrature.